Chapter 6

Applications of Bottlebrush Polymers in Functional Materials

1. Macfarlane, R. J.; Kim, B.; Lee, B.; Weitekamp, R. A.; Bates, C. M.; Lee, S. F.; Chang, A. B.; Delaney, K. T.; Fredrickson, G. H.; Atwater, H. A.; Grubbs, R. H. Improving Brush Polymer Infrared One-Dimensional Photonic Crystals via Linear Polymer Additives. *J. Am. Chem. Soc.* **2014**, *136*, 17374–17377.

2. Bates, C. M.; Chang, A. B.; Momčilović, N.; Jones, S. C.; Grubbs, R. H. ABA Triblock Brush Polymers: Synthesis, Self-Assembly, Conductivity, and Rheological Properties. *Macromolecules* **2015**, *48*, 4967–4973.

3. Bates, C. M.; Chang, A. B.; Schulze, M. W.; Momčilović, N.; Jones, S. C.; Grubbs, R. H. Brush Polymer Ion Gels. *J. Polym. Sci., Part B* **2016**, *54*, 292–300.

4. McNicholas, B. J.; Blakemore, J. D.; Chang, A. B.; Bates, C. M.; Kramer, W. W.; Grubbs, R. H.; Gray, H. B. Electrocatalysis of CO_2 Reduction in Brush Polymer Ion Gels. *J. Am. Chem. Soc.* **2016**, *138*, 11160–11163.

ABSTRACT

In the preceding chapters, we have discussed the design, synthesis, and self-assembly of graft block polymers. Robust synthetic methods have enabled the preparation of graft polymers toward a wide variety of applications in photonics,[1-3] drug delivery,[4-6] transport,[7-8] and thermoplastics.[9-10] This chapter will focus on applications of fully grafted bottlebrush block polymers as photonic crystals (Section 6-1) and solid polymer electrolytes (Section 6-2). Our work demonstrates the impacts of molecular architecture on the macroscopic properties of these materials, including the reflectivity, conductivity, and modulus. Key results have been rewritten and summarized here in order to support the central themes of this thesis: (1) ring-opening metathesis polymerization is a powerful strategy to synthesize well-defined graft polymers; (2) bottlebrush polymers have unique physical properties; and (3) these unique properties enable the design of new functional materials.

Table of Contents

6-1 Photonic Crystals

6-1.1 Introduction

Photonic crystals are ordered nanostructures that feature a periodic arrangement of domains with different refractive indices.[11-12] The spatial periodicity of the crystal determines the photonic band gap, which spans the range of frequencies in which light cannot propagate through the material. The simplest example of a photonic crystal is the one-dimensional multilayer stack. In a multilayer stack, each interface between layers reflects a certain amplitude and phase of incident light, and constructive interference results in resonant reflectivity. Traditionally, photonic crystals have been fabricated by complex top-down approaches, such as layer-by-layer deposition or co-extrusion, which require expensive equipment and limit applications to flat surfaces. The bottom-up self-assembly of bottlebrush block polymers provides an attractive alternative.

Polymer-based photonic crystals offer many advantages: they can be prepared from inexpensive materials, painted on any geometric surface, and designed to tune desired properties.[13-15] One key property of interest is the wavelength of reflection, λ. For a one-dimensional, two-component crystal, λ is determined by Bragg's law:

$$\lambda = 2(n_1 d_1 + n_2 d_2) \qquad \text{Eq. 6-1}$$

where n_i and d_i are the refractive index and thickness, respectively, of domain i.[16] Most all-organic polymers have similar $n \approx 1.5$, such that $\lambda \approx 3d^*$ (where $d^* = d_1 + d_2$ is the lamellar period). In other words, the wavelength of reflected light increases linearly with d^*. In turn, d^* is controlled by the total polymer molecular weight (*M,* Figure 6.1):

$$\lambda \sim d^* \sim M^{\alpha} \qquad \text{Eq. 6-2}$$

The scaling exponent α is typically between 1/2 and 2/3 for symmetric linear block polymers, which represent the majority of systems developed as polymer photonic crystals. In comparison, α is significantly larger for bottlebrush block polymers ($\alpha \approx 0.9$). Steric repulsion between the densely grafted side chains causes the brush backbones to adopt extended conformations;[17] further discussion of the effects of grafting density on block polymer self-assembly can be found in Chapter 3-3.

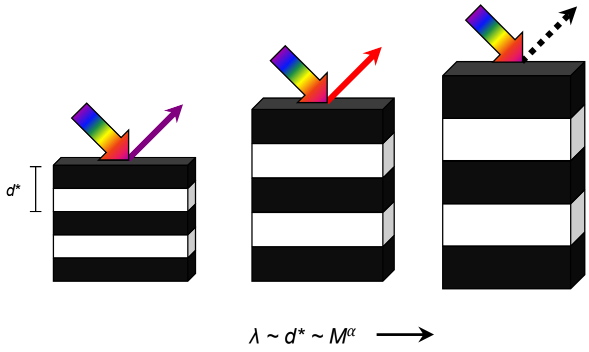

Figure 6.1: The wavelength of reflection (λ) increases linearly with the lamellar period (d^*), which in turn scales with the total block polymer molecular weight (M).

The stronger scaling of λ with M for bottlebrush polymers compared to linear polymers presents significant advantages in the context of photonic crystals. For most applications, the reflection of light at least in the visible spectrum is desired ($\lambda > 380$ nm). This requirement imposes a domain size minimum that is difficult to achieve via the synthesis and self-assembly of linear block polymers. For example, a photonic crystal that reflects blue light ($\lambda = 460$ nm) would require a linear block polymer with ultrahigh $M >$ 1 MDa.[15] The controlled synthesis of such ultrahigh-M linear block polymers is challenging, and chain entanglement presents a prohibitively high barrier to self-assembly. The unique architecture of brush polymers overcomes these challenges: λ increases strongly with M, and the extremely high entanglement molecular weights result in low viscosities[18-20] and rapid ordering kinetics.[21-22] Chapter 3-4 provides further discussion of the linear rheology of graft polymers.

Recent advances have reported the synthesis of well-defined, ultrahigh-M brush block polymers and their self-assembly to lamellar structures with unprecedentedly large domain sizes and grain sizes.[22-24] Brush block polymers can access sufficiently large d^* to reflect light throughout the visible spectrum and even into the near-infrared.[1,3,25-26] One ultimate goal is to prepare brush block polymer photonic crystals that reflect *infrared* radiation ($\lambda > 1200$ nm). These materials could be developed as heat-reflecting transparent coatings for energy-inefficient windows in buildings and other infrastructure. Reflecting infrared radiation would combat the urban heat island effect and dramatically reduce the costs and emissions associated with cooling.[27]

Despite the advantages of brush block polymers, several factors prevent potential applications from being realized in commercial settings:

1. The macromonomers required are expensive and challenging to synthesize.
2. Only short-range order is typically achieved.
3. The process does not allow post-synthetic modification to improve durability, reflectivity, and other film properties.

We have explored several design strategies to address these limitations. Three approaches will be summarized in this chapter. First, opportunities to tune d^* via the grafting density (z) will be described (Section 6-1.2). The scaling exponents α for graft block polymers with $0 << z < 1$ are typically similar to the exponent for fully grafted bottlebrush block polymers ($z = 1$); by decreasing z, less of the expensive macromonomer can be used to access similar d^*. Second, the self-assembly of polynorbornene block polymers with discrete monomers that exploit noncovalent interactions will described (Section 6-1.3). Lastly, blending graft block polymers and linear homopolymers will be described as a route to improve the optical properties of polymeric photonic crystals (Section 6-1.4).

6-1.2 Grafting Density

We recently reported the efficient synthesis of graft polymers with controlled grafting density (z), defined as the average number of polymer side chains per backbone repeat unit (Chapter 2). The scaling of d^* with the total backbone degree of polymerization depends on z, such that $d^* \sim N_{\mathrm{bb}}{}^{\alpha(z)}$ and $\alpha \sim z$ (Chapter 3-3).[17] The scaling of the zero-shear viscosity (η_0, strongly influenced by the onset of entanglements at the entanglement molecular weight, M_{e}) also affects self-assembly: ultrahigh viscosity, typical for linear polymers, leads to slower ordering kinetics and trapped metastable states. For the graft homopolymers described in Chapter 3-4, given similar N_{bb} and $M < M_{\mathrm{e}}$, the polymers have similar η_0 *regardless of grafting density.* In other words, η_0 closely tracks N_{bb}, not the number of side chains (zN_{bb}).

Combining these insights into the statics and dynamics of graft polymers guides the design of graft block polymers. Figure 6.2 provides an example. The scaling of d^* with N_{bb} for symmetric graft polymers with poly(D,L-lactide) (PLA) and polystyrene (PS) side chains was studied for $0 \leq z \leq 1$. (Further discussion can be found in Chapter 3-3.) For fully grafted bottlebrushes ($z = 1.0$), the scaling exponent α is large: $d^* \sim 1.033N_{\mathrm{bb}}{}^{0.858}$. As an illustrative example, given $N_{\mathrm{bb}} = 100$, d^* is predicted to be 54 nm (Figure 6.2A). The large domain sizes required for photonic properties can be accessed by increasing N_{bb}, but the dispersity typically increases and more of the expensive macromonomers is required. Instead of increasing N_{bb} at fixed $z = 1.0$, we can decrease the grafting density while largely retaining the advantages of the bottlebrush architecture. For example, for $z = 0.5$, α is only slightly smaller ($d^* \sim 0.926N_{\mathrm{bb}}{}^{0.815}$) and η_0 is only slightly higher. For a 50% grafted block polymer with the same side chain chemistry (PLA and PS) and same number of side chains ($zN_{\mathrm{bb}} = 100$) as the fully grafted example in Figure 6.2A, d^* is significantly larger: $d^* = 70$ nm. In other words, by using the same amount of the expensive macromonomer but decreasing z from 1.0 to 0.5, the total molecular weight M increases by only 7% but d^* increases by **30%**. This ability to increase d^* by decreasing z (using similar amounts of the expensive building blocks) introduces an attractive strategy for preparing polymeric photonic crystals.

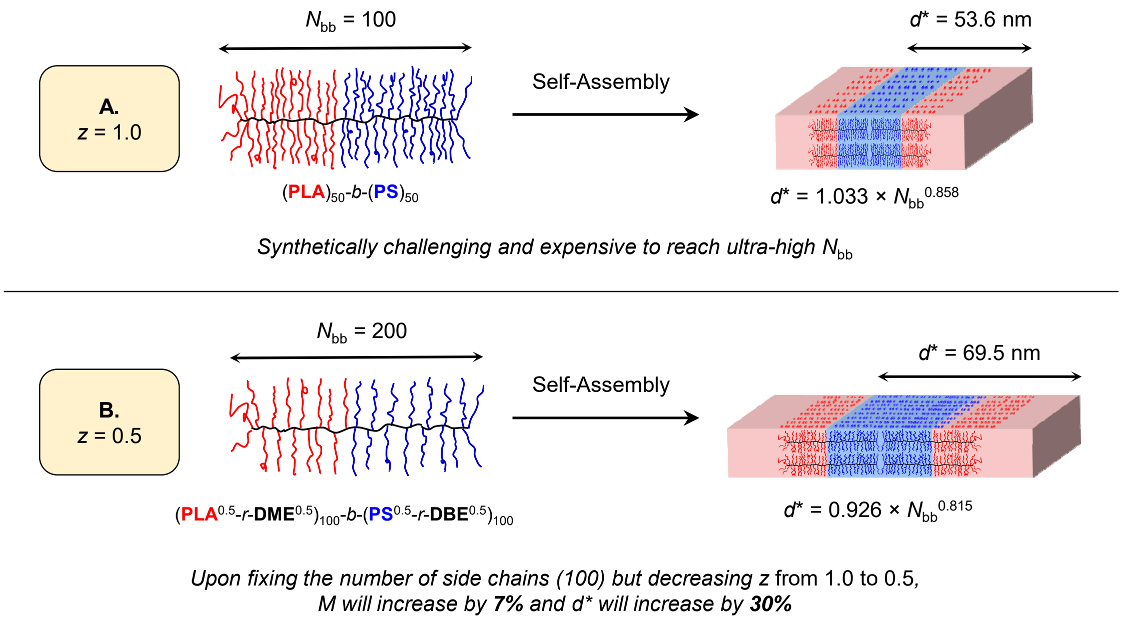

Figure 6.2: Predicted lamellar periods (d^*) for (*A*) $z = 1.0$ and (*B*) $z = 0.5$ block polymers with the same number of side chains ($zN_{\mathrm{bb}} = 100$). Comparing *A* and *B* indicates that decreasing z from 1.0 to 0.5 but maintaining the same number of side chains increases d^* by 30%.

6-1.3 Discrete Monomers

The multi-step syntheses and associated high costs of the macromonomers employed in previous approaches motivate the development of alternative building blocks. One strategy toward this goal is to design discrete monomers that promote self-assembly by templating local interactions. We synthesized three *exo*-norbornene monomers, each via a one-step amidation from commercially available starting materials. Each monomer was linked to either an octadecyl chain (C18), biphenyl group (BP), or polyhedral oligomeric silsequioxane cage (POSS). Octadecyl and biphenyl groups experience aliphatic and π-stacking interactions, respectively. POSS cages are nanosize structures with the general formula $(\mathrm{RSiO}_{1.5})_8$. The R groups offer handles to incorporate a wide variety of functionalities,[28-29] and crystallization of the cages introduces opportunities for hierarchical organization.[30] The bulky groups of the C18, BP, and POSS monomers were proposed to template domain formation in block polymers. Local interactions could potentially eliminate the need for grafted architectures in order to access long-range-ordered, large-d^* nanostructures.

Several series of POSS-*b*-C18 and C18-*b*-BP block polymers were synthesized by sequential ROMP (Scheme 6.1) The livingness, stability, and functional group tolerance of ROMP enable the synthesis of block polymers with ultrahigh total molecular weights and low dispersity. The total degree of polymerization ($N = x + y$) and the relative volume fraction of each block ($\phi_{C18} \sim y / x$) can be easily tuned; data for a representative series of POSS-*b*-C18 block polymers is provided in Table 6.1. This series targeted $x = 800$ for the first block and systematically varied the incorporation of C18, the second block. ϕ_{C18} was varied between 0.15 to 0.85, sweeping the ratios at which *linear* diblock polymers access different morphologies (including spheres, cylinders, and lamellae).

Scheme 6.1: Synthesis of block polymers with polyhedral oligomeric silsequioxane (POSS) and octadecyl (C18) side chains by sequential ROMP.

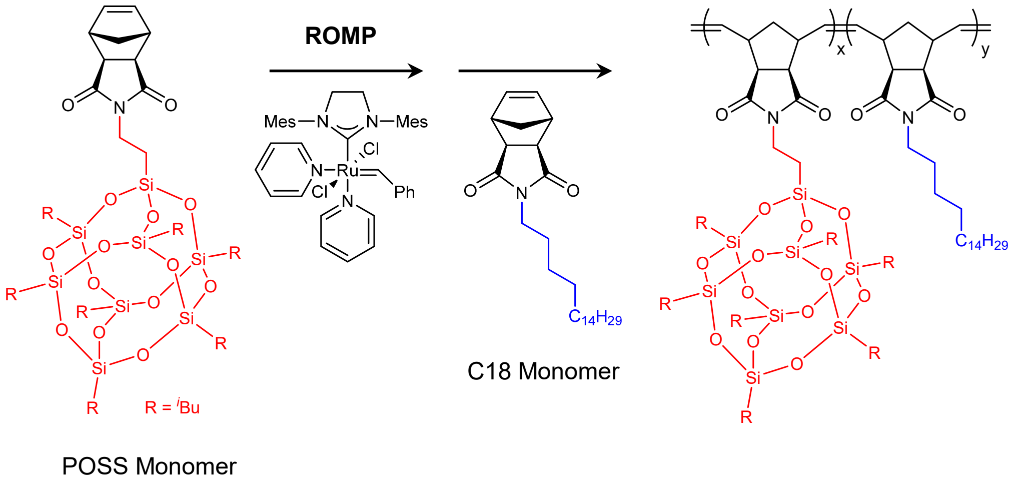

Table 6.1: Characterization data for POSS-*b*-C18 block polymers with target $x = 800$. M_w is the weight-average molecular weight, $Đ = M_w/M_n$ is the dispersity, and λ is the peak wavelength of reflected light. The morphologies were identified by scanning electron microscopy (SEM).

Entry	ϕ_{C18}	M_w (MDa)	Đ	λ (nm)	Morphology
1	0.14	1.80	1.28	—	DIS
2	0.24	2.30	1.28	670	LAM
3	0.32	2.42	1.31	590	LAM
4	0.48	3.40	1.50	510	DIS
5	0.67	2.97	1.36	—	DIS
6	0.74	2.72	1.26	—	DIS
7	0.86	2.34	1.21	—	DIS

Films of each block polymer were prepared by controlled evaporation from dichloromethane solutions. Three of the films reflected visible light: entries 2, 3, and 4 reflected orange, green, and violet light, respectively. Scanning electron micrographs (SEM) reveal lamellar morphologies (Figure 6.3). Compared to other linear block polymers, the domain sizes were large ($d^* > 200$ nm); however, compared to block polymers with polymeric or dendritic side chains,[31] the grain sizes were small. The lack of long-range order is supported by diffuse reflectance UV-vis spectrometry, which indicate very low percent reflectances for all films (<5%).

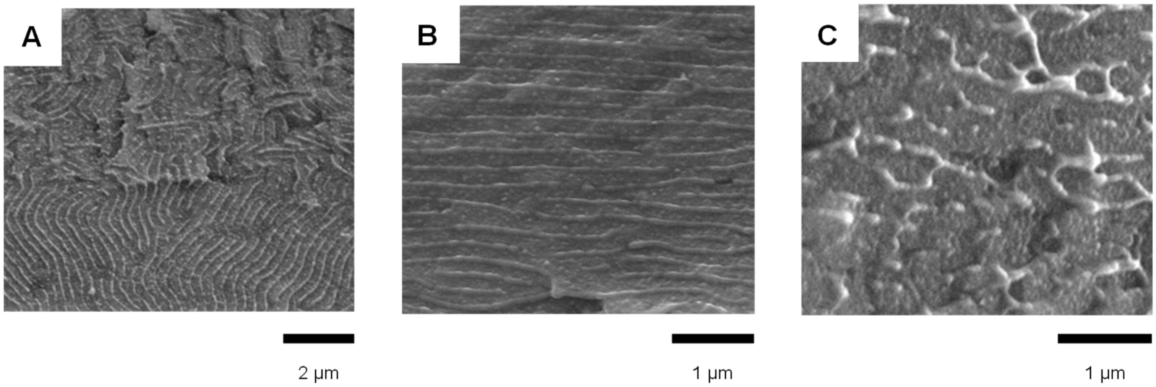

Figure 6.3: Scanning electron micrographs of cross-sections of POSS-*b*-C18 films. See Table 6.1: (*A*) Entry 2, (*B*) Entry 3, and (*C*) Entry 4. Ruthenium tetroxide (RuO_4) was used to preferentially stain POSS domains.

Like the POSS-*b*-C18 block polymers, C18-*b*-BP also lacked long-range order. These data suggest that the discrete side chains studied (and any nonspecific interactions between them) are not sufficient to promote block polymer self-assembly to photonic crystals with large d^*. We expect that these discrete groups do not to impose sufficient steric demands to extend the main chain and reduce chain entanglement. As a result, these polymers cannot achieve both the large domain sizes and long-range order displayed by graft block polymers with similar backbone lengths. Brush or brush-like building blocks may in fact be required for the rapid self-assembly of block polymers to photonic crystals that reflect light in the visible or infrared regimes.

6-1.4 Blends with Linear Homopolymers

In the preceding sections, we have discussed strategies to increase domain sizes by manipulating the polymer architecture (*i.e.*, by increasing N_{bb}, increasing z, or introducing potential templating interactions within domains). Another promising strategy to reduce the cost and improve the properties of polymeric photonic crystals is to blend graft block polymers with linear homopolymers.[32-33] Blending introduces a facile route to post-synthetically tune d^*. In addition, blending reduces the amount of expensive, architecturally complex block polymer required to reach the desired d^*. In fact, for many photonic block polymers the corresponding homopolymers are cheap commodity plastics (for example, PLA and PS), further reducing fabrication costs.

The swelling of *linear* diblock polymers with homopolymers has been extensively investigated through both theory and experiment.[34-37] We studied the swelling of *brush* diblock polymers with homopolymers (Figure 6.4).[38] Fully grafted brush block polymers with PLA (3.1 kDa) and PS (3.5 kDa) side chains were synthesized by sequential ROMP, then blended with symmetric equivalents of low-molecular-weight linear PLA and PS (M_{HP} ≈ 3 kDa).

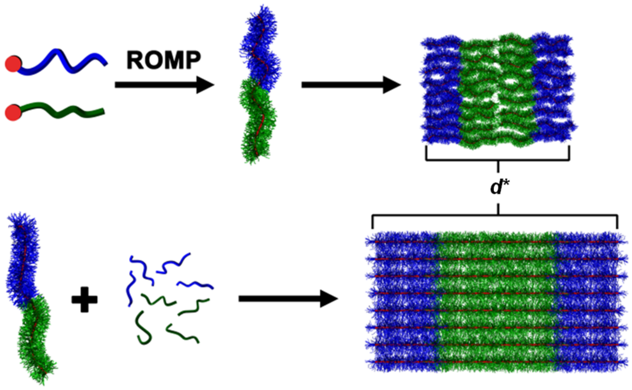

Figure 6.4: Brush block polymers self-assemble to lamellar arrays with large periods (d^*). Blending with low-molecular-weight linear homopolymers (identical to the side chains of the brush polymer) swells the structures, increasing d^*.

Blends were annealed by heating between glass slides in air for <1 minute using a heat gun (≈ 200 °C). The films were subsequently characterized by UV-visible spectrometry, scanning electron microscopy (SEM), and small-angle X-ray scattering (SAXS). Representative SEM images and plain-view photographs for a series of blends are shown in Figure 6.5A. The blends assembled to long-range ordered lamellar morphologies up to extremely high total homopolymer weight fractions ($\phi_{\mathrm{HP}} > 0.70$), and the lamellar period d^* increased monotonically with increasing ϕ_{HP} (Figure 6.5B). For a fully grafted bottlebrush with $N_{\mathrm{bb}} = 300$, blending increased d^* by up to 160% ($\phi_{\mathrm{HP}} = 0.68$), corresponding to an increase in the wavelength of reflected light from 400 nm (blue) to 530 nm (orange). Higher-molecular-weight bottlebrushes could tolerate higher ϕ_{HP}: for example, a bottlebrush with the same side chain molecular weights but $N_{\mathrm{bb}} = 530$ assembled to lamellae with $\phi_{\mathrm{HP}} = 0.73$, corresponding to a **180%** increase in d^* and λ. Above these values of ϕ_{HP}, λ decreased while reflectance peak widths increased, suggesting the onset of macrophase separation. Self-consistent field theory (SCFT) calculations indicate that each homopolymer distributes uniformly throughout domains of the same composition (*i.e.*, PLA/PLA and PS/PS), with a slight increase in relative concentrations at the centers of domains (Figure 6.5C), consistent with the behavior of linear block polymer / homopolymer blends.[34-37]

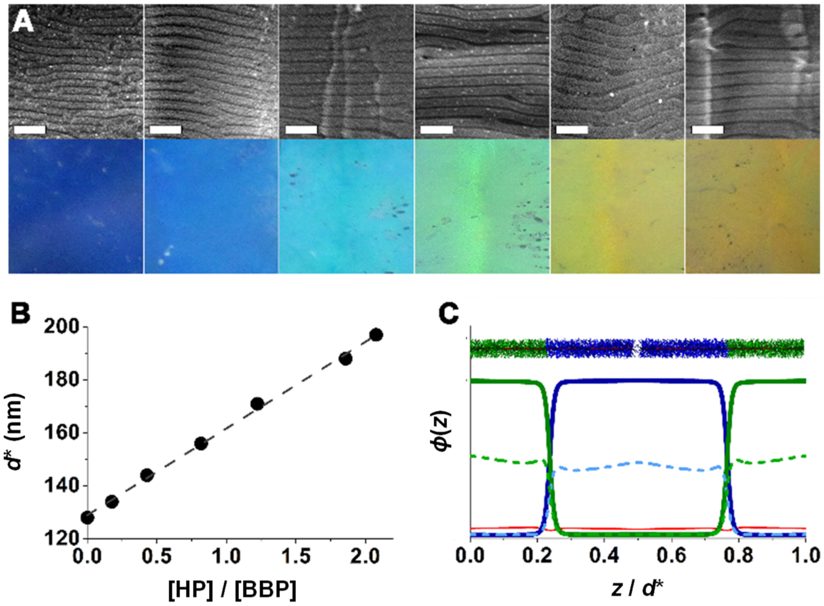

Figure 6.5: (*A*) Scanning electron micrographs of cross-sections of $(\mathbf{PLA})_{143}$-*b*-$(\mathbf{PS})_{155}$ brush block polymer films with $\phi_{\mathrm{HP}} = 0$, 0.30, 0.45, 0.55, 0.65, and 0.68 (*left to right*). Below each image is a plain-view photograph showing increasing λ with increasing ϕ_{HP}. Scale bars are 500 nm. (*B*) d^* increases with added homopolymer (HP). d^* values were obtained by SAXS and correspond to the films in *A*. (*C*) SCFT composition profile showing the relative concentrations [$\phi(z)$] of brush block polymer and HP segments within one normalized lamellar period (z / d^*). The profile corresponds to the $\phi_{\mathrm{HP}} = 0.45$ sample in *A–B*. *Blue:* PS brushes and HP; *green:* PLA brushes and HPr; *red:* polynorbornene backbone. Solid lines correspond to the brush polymer, and dashed lines correspond to HPs.

The preceding discussion has described the effects of blending linear homopolymers with fully grafted bottlebrush block polymers (z = 1). We have recently extended this work by studying blends of linear homopolymers with *graft* block polymers, where $z < 1$. The advantages of blending (this section) can be combined with the advantages of lowering the grafting density (Chapter 6-1.2) toward the large-scale fabrication of polymeric photonic crystals.

The self-assembly of graft block polymers with PLA and PS side chains was discussed in Chapter 3-3 of this thesis. Briefly: to vary z, the first block was synthesized by copolymerizing a **PLA** macromonomer (M_n = 3230 g/mol) with a discrete co-monomer, **DME** (*endo*,*exo*-norbornenyl dimethyl ester, M_n = 210 g/mol). After both co-monomers were fully consumed, a mixture of a **PS** macromonomer (M_n = 3990 g/mol) and another discrete diluent, **DBE** (*endo*,*exo*-norbornenyl di-*n*-butyl ester, M_n = 294 g/mol), was introduced as the second block. The **PS**/**DBE** feed ratio was the same as the **PLA**/**DME** feed ratio in the first block, and the reactivity ratios indicated that the copolymerization was statistically random. These $(\mathbf{PLA}^{z}\text{-}r\text{-}\mathbf{DME}^{1-z})_\mathrm{n}\text{-}b\text{-}(\mathbf{PS}^{z}\text{-}r\text{-}\mathbf{DBE}^{1-z})_n$ graft block polymers self-assembled to lamellae, where $d^* \sim N_\mathrm{bb}{}^{\alpha(z)}$ and $\alpha \sim z$.

We blended three series of graft block polymers with symmetric equivalents of linear PLA and PS homopolymers (*i.e.*, the **PLA** and **PS** macromonomers). These series — z = 0.75, 0.50, and 0.25 — correspond to entries B1–B4, C1–C4, and E1–E7 in Table 3.1. N_bb and d^* for the neat graft block polymers are reported in Table 6.2 for convenience; the fully grafted block polymers (z = 1.00, A1–A5) are included for comparison. In order to directly compare all blends, z was interpreted in terms of the backbone weight fraction (ϕ_bb). ϕ_rel indicates the backbone fraction for each series relative to ϕ_bb (z = 1.00).

Table 6.2: Graft block polymers with PLA (3230 g/mol) and PS (3990 g/mol) side chains, to be blended with linear homopolymers. The data also appear in Table 3.1.

z	ϕ_{bb}	ϕ_{rel}	**ID**	N_{bb}	d^* **(nm)**
1.00	0.028	1.0	A1	44	27.5
			A2	84	46.0
			A3	129	65.8
			A4	165	82.0
			A5	199	97.5
0.75	0.036	1.3	B1	84	40.3
			B2	130	58.2
			B3	168	72.5
			B4	219	89.5
0.50	0.052	1.9	C1	86	35.0
			C2	126	47.6
			C3	163	58.7
			C4	207	71.5
0.25	0.092	3.3	E1	90	27.9
			E2	134	36.7
			E3	153	41.5
			E4	183	47.0
			E5	197	51.5
			E6	223	55.5
			E7	262	63.5

Block polymers in each series were blended with the appropriate amounts of linear PLA and PS to match ϕ_{rel} for series with higher z. For example, polymers with $z = 0.50$ ($\phi_{rel} = 1.9$) or $z = 0.75$ ($\phi_{rel} = 1.3$) were blended with sufficient amounts of linear homopolymers to dilute the backbone concentration to $\phi_{rel} = 1.0$ (analogous to $z = 1.00$). Figure 6.6 shows the corresponding changes in d^*. Consistent with previous work on symmetric blends of fully grafted brush block polymers, d^* increases with increasing ϕ_{HP} (equivalently, *decreasing* ϕ_{rel}).

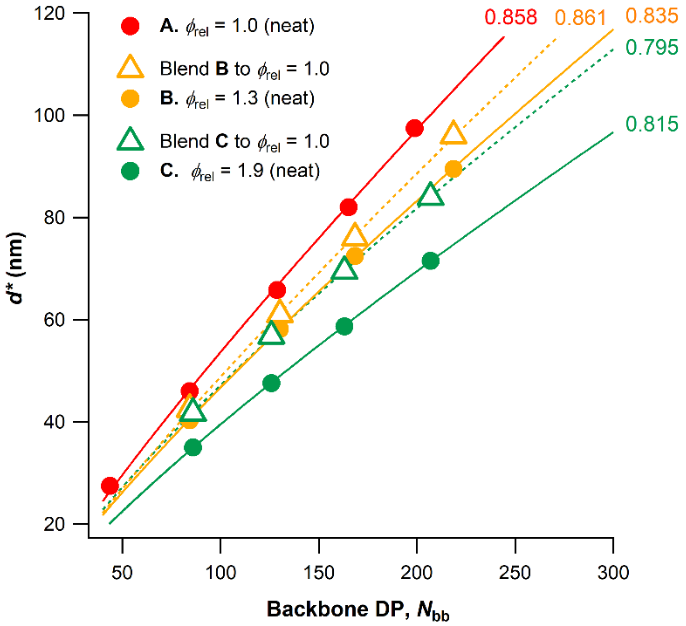

Figure 6.6: Plots of d^* versus N_{bb} for graft block polymers and blends with symmetric equivalents of linear homopolymers. ϕ_{rel} is the relative backbone concentration. **A** (*red circles*) represents neat $z = 1.00$ block polymers ($\phi_{rel} = 1.0$, A1–A5); **B** (*yellow circles*) represents neat $z = 0.75$ block polymers ($\phi_{rel} = 1.3$, B1–B4); and **C** (*green circles*) represents neat $z = 0.50$ block polymers ($\phi_{rel} = 1.9$, C1–C4). **B** and **C** were each blended with sufficient amounts of homopolymer to dilute ϕ_{rel} to 1.0 (*unfilled triangles*). Each series was fit to a power law ($d^* \sim N_{bb}{}^{\alpha}$), and the scaling exponents α are provided in the upper right corner.

Figure 6.7 compares data for blends of 25% and 50% grafted block polymers to $\phi_{rel} = 1.3$ (analogous to $z = 0.75$). The data for each blend were fitted to a power law: $d^*_{blend} \sim N_{bb}{}^{\alpha}$. For each z, α decreases monotonically with ϕ_{rel}: for example, neat $z = 0.25$ ($\phi_{rel} = 3.3$) block polymers exhibit $\alpha = 0.788$; upon blending with sufficient amounts of linear homopolymers to reach $\phi_{rel} = 1.9$ or 1.3, α decreases to 0.714 or 0.666, respectively (Figure 6.7). We note that blending from $\phi_{rel} = 3.3$ to $\phi_{rel} = 1.0$ (equivalent to $\phi_{HP} = 0.72$) results in disordered materials rather than lamellar morphologies. However, the observation that blending $\phi_{rel} = 3.3$ to $\phi_{rel} = 1.9$ (equivalent to $\phi_{HP} = 0.62$) *does* produce lamellar morphologies suggests that low-z block polymers can tolerate large amounts of incorporated homopolymers. Fully grafted ($z = 1.00$) bottlebrushes with identical side chain chemistries (PLA, PS) and molecular weights (≈ 3 kDa) also disorder when $\phi_{HP} > 0.70$.[38] These trends expand previous insights into the impact of grafting density on block polymer self-assembly. Ongoing work aims to further understand how the molecular architecture affects the ordering kinetics and scaling of d^* in blends.

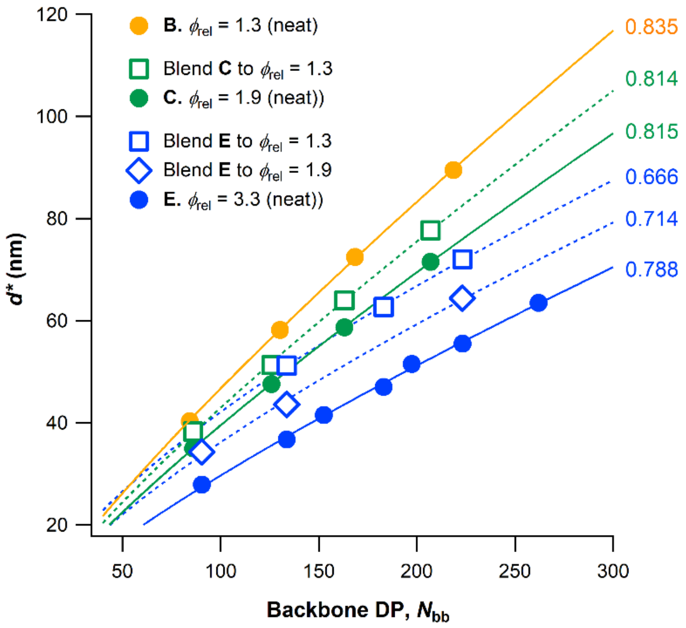

Figure 6.7: Plots of d^* versus N_{bb} for graft block polymers and blends with symmetric equivalents of linear homopolymers. ϕ_{rel} is the relative backbone concentration. **B** (*yellow circles*) represents neat $z = 0.75$ block polymers ($\phi_{rel} = 1.3$, B1–B4); **C** (*green circles*) represents neat $z = 0.50$ block polymers ($\phi_{rel} = 1.9$, C1–C4); and **E** (*blue circles*) represents neat $z = 0.25$ block polymers ($\phi_{rel} = 3.3$, E1–E7). **C** and **E** were each blended with sufficient amounts of homopolymer to dilute ϕ_{rel} to 1.3 (*unfilled squares*); **E** was also blended to reach $\phi_{rel} = 1.9$ (*unfilled diamonds*). Each series was fit to a power law ($d^* \sim N_{bb}^{\alpha}$), and the scaling exponents α are provided on the right.

6-2 Solid Polymer Electrolytes

6-2.1 Introduction

Batteries require electrolytes that facilitate the reversible movement of charges and physically separate the anode and cathode. Lithium ion batteries typically contain highly conductive liquid electrolytes that suffer from potential safety issues due to lithium dendrite grown and the use of flammable small molecule solvents. Solid polymer electrolytes (SPEs) are promising alternatives to conventional liquid electrolytes.[39-40] The ideal SPE exhibits both high ionic conductivity and a high modulus: the key challenge is to achieve high mechanical and thermal performance without sacrificing ionic conductivity. By far the most widely used conductive component is amorphous poly(ethylene oxide) (PEO), which dissolves lithium salts and enables the movement of lithium cations by cooperative polymer segmental relaxation.[41] Unfortunately, rubbery materials such as amorphous PEO lack the mechanical integrity necessary for application in polymer electrolyte membranes (PEMs), and as a consequence, many strategies have been explored to improve PEM stiffness (typically by copolymerization and/or crosslinking). With few exceptions,[42] conductivity and modulus are generally inversely related: highly conductive materials are structurally weak (*e.g.*, fluids), while stiff materials are typically non-conductive (*e.g.*, polymer glasses).

Block polymers provide successful strategies to decouple these properties. AB diblock and ABA triblock copolymers — in which block A is a glassy, rigid insulator and block B is a rubbery conductor — allow the mechanical properties and conductivity to be independently tuned. Many polymer architectures have been studied to date.[43-44] The most prevalent of these materials is linear poly(styrene-*block*-ethylene oxide), PS-*b*-PEO, which generally offers modest conductivity ($\leq 10^{-3}$ S/cm at 90 °C) and promising elastic moduli approaching 10^8 Pa.[45-46]

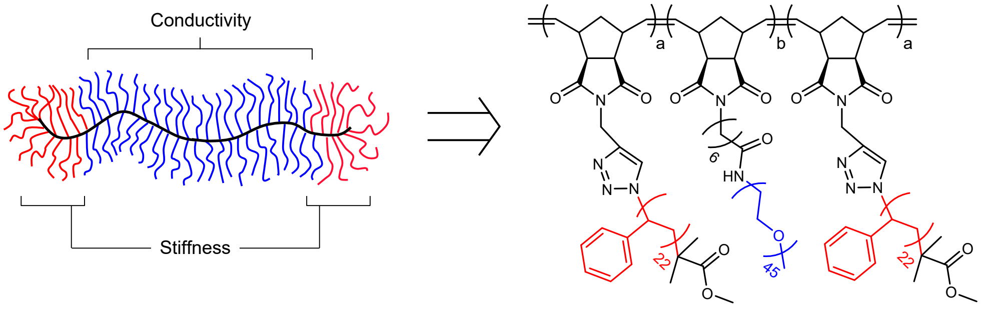

Figure 6.8: (*left*) Schematic illustration and (*right*) chemical structure of *g*PS-*g*PEO-*g*PS (SOS) brush triblock copolymers.

In this chapter, we describe the synthesis, characterization, and initial SPE applications of well-defined bottlebrush triblock copolymers, designated *g*PS-*g*PEO-*g*PS (SOS) (Figure 6.8). Section 6-2.2 will discuss the properties of blends of SOS brush triblock copolymers with lithium salt. The normalized conductivity improves but the modulus decreases relative to linear PS-*b*-PEO-*b*-PS and PS-*b*-PEO analogues. Section 6-

2.3 will discuss blends of SOS with ionic liquids, forming physically crosslinked ion gels, as well as applications of these materials as solid supports for electrocatalysis. Reflecting the themes of this thesis, we will highlight the impact of the brush architecture on the self-assembly and properties of these materials.

6-2.2 Blends with Lithium Salt

Brush *g*PS-*g*PEO-*g*PS triblock copolymers were synthesized by sequential ring-opening metathesis polymerization (ROMP) (PS: $M_n = 2.5$ kDa; PEO: $M_n = 2.0$ kDa). Four triblocks with different absolute and relative backbone degrees of polymerization for the PS and PEO blocks were synthesized (Table 6.3).

Table 6.3: Characterization data for $g\mathrm{PS}_a$-$g\mathrm{PEO}_b$-$g\mathrm{PS}_a$ brush triblock copolymers.

Sample	$N_{\mathrm{bb,i}}$[a]	M_n[b] (kDa)	$Đ$[b]	ϕ_{PS}[c]
$g\mathrm{PS}_3$-$g\mathrm{PEO}_{85}$-$g\mathrm{PS}_3$	3-85-3	208	1.05	0.077
$g\mathrm{PS}_6$-$g\mathrm{PEO}_{87}$-$g\mathrm{PS}_5$	6-87-5	225	1.12	0.12
$g\mathrm{PS}_{11}$-$g\mathrm{PEO}_{78}$-$g\mathrm{PS}_{11}$	11-78-11	234	1.17	0.24
$g\mathrm{PS}_{15}$-$g\mathrm{PEO}_{119}$-$g\mathrm{PS}_{15}$	15-119-15	348	1.08	0.22

[a] Backbone degrees of polymerization for each block *i*.
[b] Determined by size-exclusion chromatography in tetrahydrofuran with 1 vol% trimethylamine.
[c] PS volume fraction calculated using $\rho_{\mathrm{PS}} = 1.05$ g/cm^3 and $\rho_{\mathrm{PEO}} = 1.06$ g/cm^3.

Blends of these brush block polymers and lithium bis(trifluoromethylsulfonyl)imide (LiTFSI) were subsequently prepared with different [EO]:[Li$^+$] ratios, calculated as the average total number of ethylene oxide repeat units per chain relative to moles of LiTFSI. Differential scanning calorimetry (DSC) reveals a monotonic increase in the glass transition temperature (T_g) of PEO with increasing LiTFSI concentration (*i.e.*, *decreasing* [EO]:[Li$^+$]) (Figure 6.9). The observed increase in T_g with increasing salt concentration reflects the reduction in chain mobility due to polymer-ion interactions and transient crosslinking. Under the DSC conditions (ramp rates of 5, 10, and 20 °C/min), PEO crystallization was suppressed for [EO]:[Li$^+$] = 2:1, 5:1, and 10:1 for both $g\mathrm{PS}_{11}$-$g\mathrm{PEO}_{78}$-$g\mathrm{PS}_{11}$ and $g\mathrm{PS}_{15}$-$g\mathrm{PEO}_{119}$-$g\mathrm{PS}_{15}$. For the former (lower N_{bb}), crystallization suppression was additionally observed for [EO]:[Li$^+$] = 15:1. Although no evidence of crystallization was observed on the timescales of the DSC measurements, both $g\text{PS}_{11}$-$g\text{PEO}_{78}$-$g\text{PS}_{11}$/LiTFSI (15:1) and $g\text{PS}_{15}$-$g\text{PEO}_{119}$-$g\text{PS}_{15}$/LiTFSI (10:1) blends exhibited clear melting transitions after aging for two months at room temperature, indicating arrested crystallization kinetics. All other samples remained unchanged.

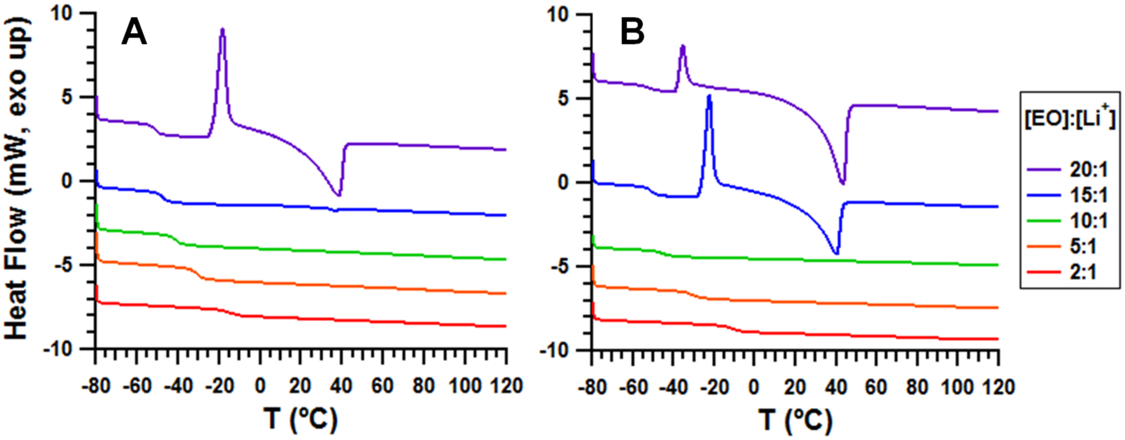

Figure 6.9: Differential scanning calorimetry data for SOS brush triblock copolymers as functions of LiTFSI loading: (*A*) $g\text{PS}_{11}$-$g\text{PEO}_{78}$-$g\text{PS}_{11}$ and (*B*) $g\text{PS}_{15}$-$g\text{PEO}_{119}$-$g\text{PS}_{15}$. Traces are shown for a 5 °C/min ramp rate on heating and are shifted vertically for clarity.

Since Li^+ diffusion usually occurs exclusively in amorphous PEO (*i.e.*, not in crystalline domains), preventing crystallization is crucial for PEM applications. Various strategies have addressed this issue, including using lithium salt mixtures[47] and (meth)acrylates functionalized with low-molecular-weight oligo-PEO side chains.[48-51] Our brush SOS/LiTFSI blends ($N_{\text{PEO}} = 45$) demonstrate a surprising tendency to avoid crystallization considering oligo-PEO acrylate derivatives with side chain degrees of polymerization $N_{\text{PEO}} \geq 7$ typically show incipient crystallization.[49] In addition, blends of linear PEO homopolymer ($N_{\text{PEO}} \approx 90$) with LiTFSI display relatively small crystallinity gaps ($6 < [\text{EO}]:[\text{Li}^+] < 12$)[52] compared to brush SOS/LiTFSI blends (see Figure 6.9A, $2 < [\text{EO}][\text{Li}^+] < 15$). DSC measurements performed for blends of the PEO macromonomer ($N_{\text{PEO}} = 45$) and LiTFSI are consistent with the crystallinity gap reported for brush SOS; in other words, the side chains in the *g*PEO brush behaves in the same way as a linear PEO homopolymer with the same molecular weight. The suppression of crystallization over this range of lithium salt concentrations highlights one advantage of the brush architecture:

high-molecular-weight brush polymers (large *a*, *b*) bearing low-molecular-weight grafted PEO side chains (N_{PEO}) appear to minimize crystallization, since crystallinity generally increases with N_{PEO} and evidently not the backbone degree of polymerization (*b*).

The polymer architecture may also affect the kinetics of brush polymer crystallization. Previous reports of the crystallization of brush poly(L-lactide) (PLLA) homopolymers reveal an Avrami exponent (*n*) approaching 2, in contrast to linear PLLA ($n \approx 4$). The lower exponent observed for brush PLLA suggests considerably slower crystallization kinetics and lower equilibrium melting temperatures (*i.e.*, more crystal defects).[53] Combining the graft and block architectures therefore combines the advantages of crystallization suppression with the potential to decouple conductive and mechanical properties.

AC impedance spectroscopy was used to measure conductivity (σ) as a function of [EO]:[Li$^+$]. Because LiTFSI is highly hygroscopic, all sample preparation was performed in a dry room to eliminate moisture contamination. Conductivity increases with [EO]:[Li$^+$] up to moderate blend ratios (10:1–20:1), since the number of charge carriers increases with salt concentration. However, conductivity decreases upon further increasing the salt concentration, consistent with saturating EO binding motifs and reducing chain mobility. Figure 6.10 plots the normalized conductivity ($\sigma/\sigma_{\text{max}}$) versus temperature for [EO]:[Li$^+$] = 2:1, 5:1, and 10:1. σ_{max} corresponds to the conductivity of a linear 300 kDa PEO homopolymer and is defined, analogous to previous reports,[45] as the measured conductivity of homo-PEO (σ_{PEO}) moderated by the volume fraction of PEO in the block polymer (ϕ_{PEO}) and a morphology factor ($0 \leq f \leq 1$) related to the continuity of the conducting phase:

$$\sigma_{\text{max}} = f\sigma_{\text{PEO}}\phi_{\text{PEO}} \qquad \text{Eq. 6-3}$$

SAXS measurements identified hexagonally packed cylindrical morphologies for all blends, dictating continuous PEO domains ($f = 1$).[41] The normalized conductivities in Figure 6.10 are remarkably large for 2 kDa PEO chains. (Normalization with literature-reported σ values for 4 kDa linear PEO[52] reduces $\sigma/\sigma_{\text{max}}$ by 50% but reaches the same conclusion.) For comparable *linear* PS-*b*-PEO, $\sigma/\sigma_{\text{max}} < 0.1$ [46,54] and reaches 0.3 only when $M_{\text{PEO}} \approx 40$ kDa.[45] Instead, the values for brush SOS more closely resemble those for ultralow-M_{PEO} disordered PS-*b*-PEO.[55] $\sigma/\sigma_{\text{max}} \approx 1$ suggests differences between the graft and linear block polymer architectures involving Li^+ diffusion, wherein the graft block polymers more closely mimic PEO homopolymers.

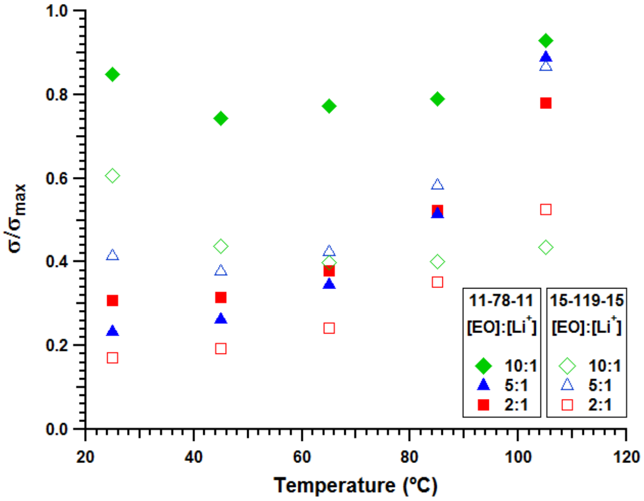

Figure 6.10: Normalized ionic conductivity (σ/σ_{max}) for gPS$_{11}$-gPEO$_7$-gPS$_{11}$/LiTFSI and gPS$_{15}$-gPEO$_{119}$-gPS$_{15}$/LiTFSI blends, relative to linear PEO (M_n = 300 kDa).

The SOS brush triblock copolymers display similar or moderately higher conductivity than linear PEO-containing block polymers (*e.g.*, PS-*b*-PEO,[46] PS-*b*-PEO-*b*-PS,[56] and PP-*b*-PEO-*b*-PP[57]). The comparable conductivity is perhaps surprising, since the brush architecture dilutes the volume fraction of the conducting PEO domain with the polynorbornene backbone (by ≈ 10% for gPS$_{11}$-gPEO$_{78}$-gPS$_{11}$), previously assumed to *decrease* conductivity.[43] Other architecture effects may compensate for dilution by the backbone, such as low melt viscosity,[18-20] altered lithium ion distribution in brush PEO domains,[58] chain end effects,[59] ionic interactions,[60] and/or conductive domain grain sizes.[61] We also note that the conductivity of these SOS brush triblock copolymers appears to decrease with b, the backbone degree of polymerization of the gPEO block; in stark contrast, the conductivity of linear PEO-containing block polymers dramatically *increases* with increasing N_{PEO}.[45-46] Ongoing work aims to elucidate the physical mechanisms underlying the relationships between conductivity and polymer architecture.

Frequency-dependent melt rheology data are reported in Figure 6.11 for gPS$_{11}$-gPEO$_{78}$-gPS$_{11}$. Between 0.01 and 100 rad/s, at temperatures 45–105 °C, the storage modulus (G') is on the order of 10^4 Pa and is always larger than the loss modulus (G'').

Time-temperature superposition of the relaxation spectra fails; the data are therefore reported as isothermal frequency sweeps. *g*PS$_{11}$-*b*-*g*PEO$_{78}$-*b*-*g*PS$_{11}$ is a viscoelastic solid and considerably softer than linear PS-*b*-PEO ($G' \sim 10^7$ Pa at 90 °C for $\phi_{\mathrm{PEO}} = 0.38$).[45] Based on reports of linear PS-*b*-PEO,[45] the brush SOS/Li$^+$ blends should be more elastic (perhaps by an order of magnitude), but the relative softness is likely an inevitable limitation of the brush architecture.[51,62]

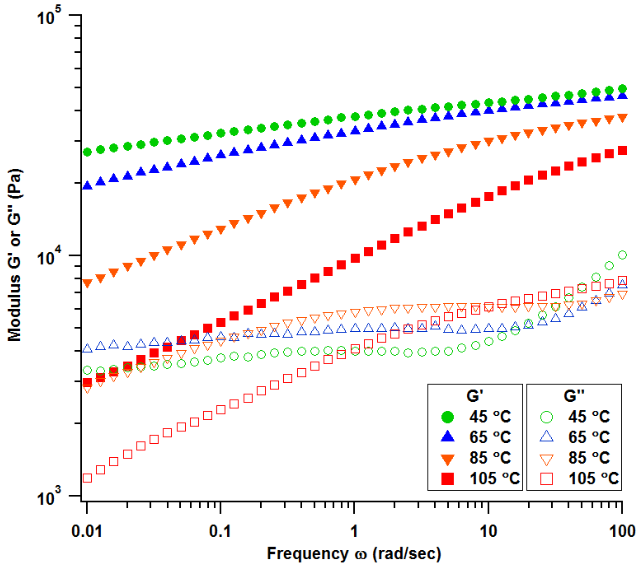

Figure 6.11: Dynamic mechanical analysis of neat *g*PS$_{11}$-*g*PEO$_{78}$-*g*PS$_{11}$, presenting the storage (G') and loss (G'') moduli as functions of temperature and frequency (ω).

Table 6.4 compares ABA linear and bottlebrush polymer architectures in terms of the conductivity and modulus, two key properties of solid polymer electrolytes. The normalized conductivity ($\sigma / \sigma_{\mathrm{max}}$) is typically higher for brush polymers, while the storage modulus (G') is typically higher for linear polymers. Further advances are required in order to maximize both the conductivity and modulus. Combining the brush block polymer architecture with techniques such as polymerization-induced phase separation[42] may provide routes towards stiffer materials while retaining the advantages of higher normalized conductivities.

Table 6.4: Comparison of linear and brush polymer architectures in terms of the normalized conductivity ($\sigma / \sigma_{\max}$) and storage modulus (G').

	 **ABA Linear Polymer**	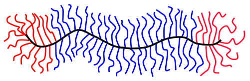 **ABA Brush Polymer**
Conductivity (σ/σ_{max})	≤ 0.3	≤ 0.9
Modulus (G', Pa)	~ 10^7	~ 10^4

6-2.3 Brush Polymer Ion Gels

In addition to blends of brush SOS triblock copolymers with LiTFSI, we have also studied blends of brush SOS with ionic liquids (IL).[8] Block polymers containing IL have emerged as promising alternative electrolytes for lithium batteries.[63-65] ILs are room-temperature molten salts composed mostly of organic ions. Their unique combination of properties — including reduced flammability, low vapor pressure, exceptional thermal and electrochemical stability, low toxicity, and high ionic conductivity — make them attractive materials for battery applications.[66-67] Toward integration in devices, providing ILs with mechanical integrity without sacrificing ionic conductivity is desired. Ion gels (*i.e.*, SPEs incorporating ILs) are advantageous due to their high ionic conductivity (~10^{-3} S/cm at 25 °C)[68] compared to conventional lithium salt SPEs such as PEO/$LiClO_4$ (~10^{-5} S/cm at 25 °C).[69]

The network structure of the ion gel can be formed either by chemically reacting monomers with functional crosslinkers or by creating physically associated crosslinks. The physical crosslinking of block polymers is a particularly versatile strategy due to the synthetic ease of tuning the gel structure and properties via block lengths and sequences. In the presence of IL, an ABA triblock copolymer with *ionophobic* A blocks and an *ionophilic* B block self-assembles to a network in which micelles of A are bridged by B blocks and dispersed in a continuous B/IL phase.[45,70] We have exploited this phenomenon to fabricate brush polymer ion gels (Figure 6.12A). The *g*PS-*g*PEO-*g*PS brush triblock copolymers described in Section 6-2.2 (Table 6.3) were gelled in 1-butyl-3-

methylimidazolium bis(trifluoromethylsulfonyl)imide ([BMI][TFSI]) at polymer concentrations spanning $0.05 < \phi_{\mathrm{SOS}} < 0.5$. SAXS measurements of the ion gels confirms a disordered micellar structure (Figure 6.12B).

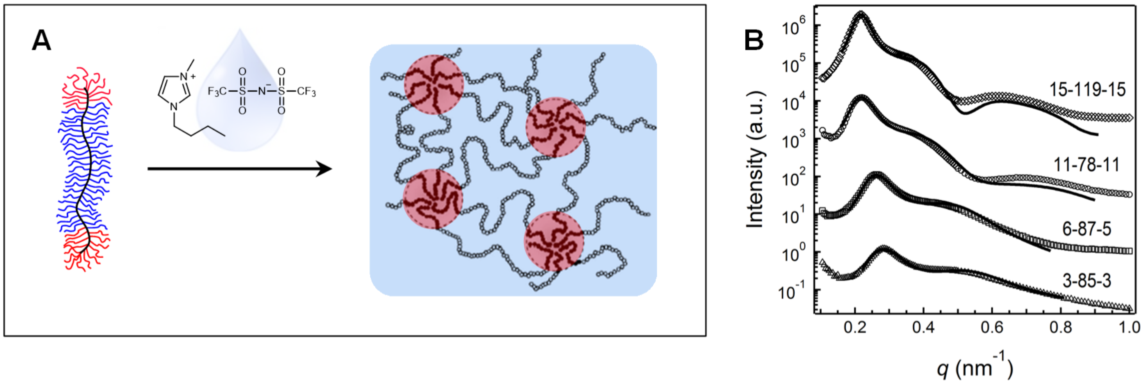

Figure 6.12: (*A*) Brush polymer ion gels were prepared by blending *g*PS-*g*PEO-*g*PS brush triblock copolymers with an ionic liquid, [BMI][TFSI]. Disordered micelles of *g*PS in a continuous matrix of *g*PEO and [BMI][TFSI] result. (*B*) Azimuthally averaged small-angle X-ray scattering data from four different *g*PS-*g*PEO-*g*PS brush block polymers at polymer concentrations $\phi_{\mathrm{SOS}} = 0.33$. The backbone degrees of polymerization for each block are provided. Solid block lines represent fits to a model using a hard sphere form factor and Percus-Yevick structure factor. Traces are shifted vertically for clarity.

As in our study of polymer/Li$^+$ blends, we aim to (1) study the conductivity and rheological properties of these materials and (2) understand the impact of the brush polymer architecture. Frequency-dependent rheology data are provided in Figure 6.13 for ion gels containing $\phi_{\mathrm{SOS}} = 0.16$ *g*PS$_3$-*g*PEO$_{85}$-*g*PS$_3$ or *g*PS$_{15}$-*g*PEO$_{119}$-*g*PS$_{15}$ in [BMI][TFSI]. The two samples display markedly different viscoelastic behavior, which we attribute primarily to the different *g*PS backbone lengths. For *g*PS$_{15}$-*g*PEO$_{119}$-*g*PS$_{15}$ ($\phi_{g\mathrm{PS}} = 0.22$), the storage modulus ($G'$) remains constant ($\approx 10^3$ Pa) at frequencies 0.01–100 rad/sec and temperatures 25–85 °C. In contrast, *g*PS$_3$-*g*PEO$_{85}$-*g*PS$_3$ ($\phi_{g\mathrm{PS}} = 0.077$) transitions from a solid-like ($G' > G''$) to liquid-like ($G' < G''$) response at 25°C on the order of 10^2 sec, which decreases by at least four orders of magnitude as the temperature increases to 85 °C (data not shown). The strong dependence of modulus and relaxation time on end-block length, polymer composition, and/or temperature is also observed with linear ABA block copolymer gels.[71] The energetic penalty for chain pullout (a stress relaxation mechanism) is controlled by the interaction parameter $\chi_{g\mathrm{PS/IL}}$, characterizing the unfavorable interactions between the gPS end blocks and IL. Typical mixtures exhibit upper critical solution behavior ($\chi \sim T^{-1}$), such that the components become more miscible as the temperature increases. In contrast, increasing the gPS molecular weight (M_A) should disfavor mixing since the ideal combinatorial entropy of mixing scales as $\Delta S_{mix} \sim M_A^{-1}$. Midblock entanglements also significantly influence the modulus and relaxation of ABA triblock copolymers and their corresponding gels. Although the grafted PEO side-chains are slightly longer than their entanglement molar mass (M_e = 1.6 kDa),[72] the brush architecture suppresses entanglements,[73] decreasing the elastic modulus of bulk brush polymers relative to linear analogues.[19,62,74] This trend also holds for gels; a linear PS-*b*-PEO-*b*-PS ion gel ($\phi_{PS} \approx 0.07$) exhibits frequency-dependent elastic moduli approximately 10^1–10^2 Pa larger than the similar gPS$_3$-gPEO$_{85}$-gPS$_3$ brush block polymers reported herein.[75]

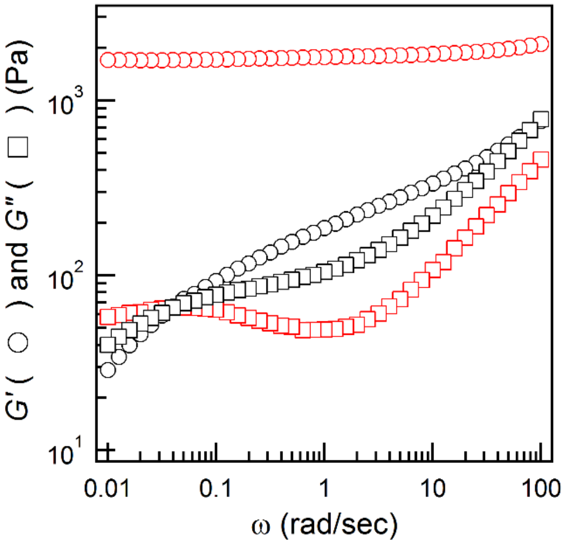

Figure 6.13: Dynamic mechanical analysis of ϕ_{SOS} = 0.16 ion gels containing gPS$_{15}$-gPEO$_{119}$-gPS$_{15}$ (*red*) or gPS$_3$-gPEO$_{85}$-gPS$_3$ (*black*) at 25 °C, presenting the storage (G') and loss (G'') moduli as functions of frequency (ω).

The ionic conductivity (σ) of the brush polymer ion gels was probed using AC impedance spectroscopy over the temperature range 25–95°C. Conductivities (~1 mS/cm at 25°C) are comparable to ion gels derived from linear triblock copolymers[75] and represent a considerable increase relative to dry linear[45] and brush[7] electrolytes. Conductivity generally decreases as polymer concentration increases due to an increase in T_g and concomitant decrease in ion mobility, a trend also found with both chemically[76] and physically[77] cross-linked linear polymer gels. Normalized conductivities (σ/σ_{max}, relative to neat [BMI][TFSI]) are provided in Figure 6.14 for *g*PS$_3$-*g*PEO$_{85}$-*g*PS$_3$ and *g*PS$_{15}$-*g*PEO$_{119}$-*g*PS$_{15}$ gels. The relatively high conductivities ($0.2 < \sigma/\sigma_{max} < 0.8$) highlight the liquid-like order in the gel phase, consistent with measurements obtained for linear analogues. The conductivity decreases with increasing *a*:*b* backbone block ratios and polymer concentration but generally remains near neat [BMI][TFSI].

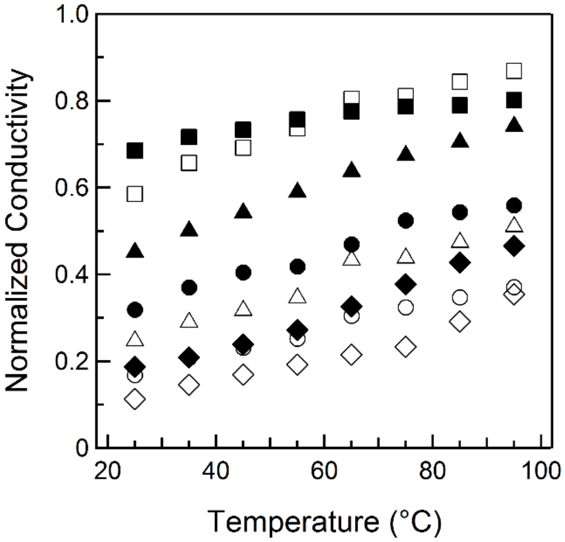

Figure 6.14: Ionic conductivities for brush polymer ion gels, normalized to neat [BMI][TFSI]. Closed and open symbols represent *g*PS$_3$-*g*PEO$_{85}$-*g*PS$_3$ and *g*PS$_{15}$-*g*PEO$_{119}$-*g*PS$_{15}$ samples, respectively. Polymer concentrations are 9 (□ and ■), 16 (△ and ▲), 23 (○ and ●), and 29 wt% (◊ and ♦).

In addition to studying the conductivity and rheological properties of ion gels, we have recently demonstrated that ion gels are attractive solid supports for electrocatalysis.[78] *g*PS$_{15}$-*g*PEO$_{119}$-*g*PS$_{15}$ in [BMI][TFSI] was mixed with some combination of ferrocene (Fc), cobaltocenium ($CoCp_2^+$), and Re(bpy)$(CO)_3$Cl (Figure 6.15). The physically crosslinked polymer networks decouple the molecular interactions providing macroscopic solid-like mechanical properties from the electrochemical activity of the homogenous small-molecule catalysts. This design captures the benefits of a solid support without requiring catalyst redesign and/or surface attachment. The electroactive small molecules dissolved in the *g*PEO / [BMI][TFSI] matrix domain are capable of undergoing redox reactions due to the high ionic conductivity and polarizability of the IL medium. Incorporating Re(bpy)(CO)$_3$Cl, a well-established CO$_2$ reduction catalyst,[79-81] enables useful electrochemical reactions with homogenous catalysts exhibiting macroscopic solid-like properties.

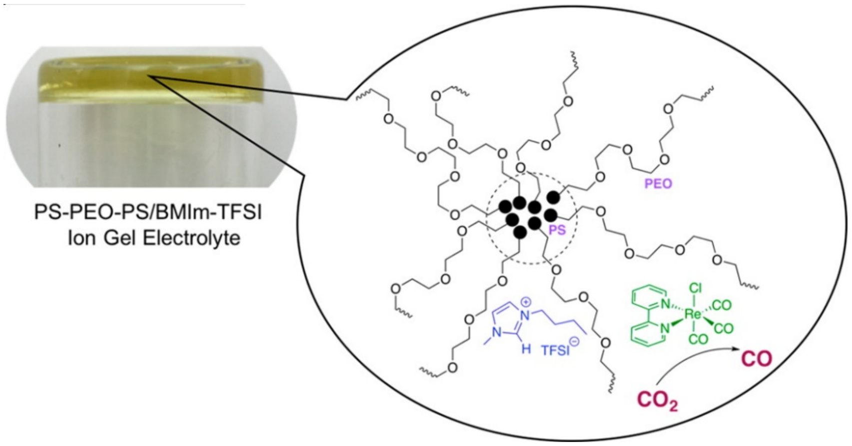

Figure 6.15: Electrocatalytic reduction of CO$_2$ to CO in *g*PS-*g*PEO-*g*PS brush polymer ion gels. The catalyst, Re(bpy)(CO)$_3$Cl, dissolves in the continuous *g*PEO / [BMI][TFSI] matrix.

The brush polymer ion gels exhibited diffusion-controlled redox processes with diffusion coefficients approximately one-fifth of those observed in neat [BMI][TFSI]. In gels containing Fc, Re(bpy)(CO)$_3$Cl, and 1 atm CO$_2$, a catalytic wave was observed (Figure 6.16). The catalytic wave exhibits a sizeable, positive shift compared to analogous non-aqueous solvents with a reduction potential 500 mV positive of onset and 90% Faradaic efficiency.

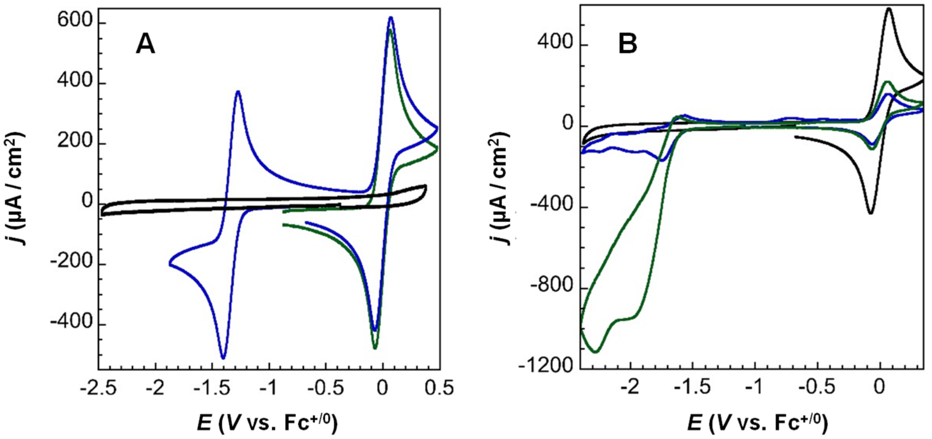

Figure 6.16: Cyclic voltammetric scans of brush polymer ion gels comprising *g*PS$_{15}$-*g*PEO$_{119}$-*g*PS$_{15}$, [BMI][TFSI]. (*A*) Ion gels containing no additives (*black*); 14.3 mM Fc (*green*); or 14.3 mM Fc and 15.3 mM CoCp$_2^+$ (*blue*). (*B*) Ion gels containing 14.3 mM Fc and 1 atm CO$_2$ (*black*); 5 mM Fc and 10 mM Re(bpy)(CO)$_3$Cl (*blue*); or 7.1 mM Fc, 14.3 mM Re(bpy)(CO)$_3$Cl, and 1 atm CO$_2$ (*green*).

Brush polymer ion gels represent valuable platforms that bridge the gap between homogenous, solution-state catalysis and heterogeneous, solid-state catalysis. This new class of materials is capable of electrocatalytically reducing CO$_2$ with a well-defined, small-molecule catalyst typically used in homogenous solutions. The catalytic enhancement and high CO$_2$ solubility imparted by the ionic liquid results in a significant decrease in CO$_2$ reduction potential compared to other non-aqueous electrolytes. Since physical crosslinks imbue mechanical properties, reversible gelation is thermally accessible. Extraction of electrochemical reaction products, macroscopic shape adjustment, and repeated recycling should therefore be possible. These advances are all crucially enabled by the graft polymer molecular architecture.

6-3 References

(1) Liberman-Martin, A. L.; Chu, C. K.; Grubbs, R. H. *Macromol. Rapid Commun.* **2017**, *38*, 1700058.

(2) Runge, M. B.; Bowden, N. B. *J. Am. Chem. Soc.* **2007**, *129*, 10551–10560.

(3) Sveinbjörnsson, B. R.; Weitekamp, R. A.; Miyake, G. M.; Xia, Y.; Atwater, H. A.; Grubbs, R. H. *Proc. Natl. Acad. Sci. U.S.A.* **2012**, *109*, 14332–14336.

(4) Qiu, L. Y.; Bae, Y. H. *Biomaterials* **2007**, *28*, 4132–4142.

(5) Johnson, J. A.; Lu, Y. Y.; Burts, A. O.; Lim, Y.-H.; Finn, M. G.; Koberstein, J. T.; Turro, N. J.; Tirrell, D. A.; Grubbs, R. H. *J. Am. Chem. Soc.* **2011**, *133*, 559–566.

(6) Bhattarai, N.; Ramay, H. R.; Gunn, J.; Matsen, F. A.; Zhang, M. *J. Control. Release* **2005**, *103*, 609–624.

(7) Bates, C. M.; Chang, A. B.; Momčilović, N.; Jones, S. C.; Grubbs, R. H. *Macromolecules* **2015**, *48*, 4967–4973.

(8) Bates, C. M.; Chang, A. B.; Schulze, M. W.; Momčilović, N.; Jones, S. C.; Grubbs, R. H. *J. Polym. Sci., Part B: Polym. Phys.* **2016**, *54*, 292–300.

(9) Jiang, F.; Wang, Z.; Qiao, Y.; Wang, Z.; Tang, C. *Macromolecules* **2013**, *46*, 4772–4780.

(10) Zhang, J.; Schneiderman, D. K.; Li, T.; Hillmyer, M. A.; Bates, F. S. *Macromolecules* **2016**, *49*, 9108–9118.

(11) Joannopoulos, J. D.; Johnson, S. G.; Winn, J. N.; Meade, R. D. *Photonic Crystals: Molding the Flow of Light*; 2nd ed.; Princeton University Press: Princeton, NJ, 2008.

(12) Yablonovitch, E. *J. Phys.: Condens. Matter* **1993**, *5*, 2443.

(13) Fink, Y.; Urbas, A. M.; Bawendi, M. G.; Joannopoulos, J. D.; Thomas, E. L. *J. Lightwave Technol.* **1999**, *17*, 1963.

(14) Edrington, A. C.; Urbas, A. M.; DeRege, P.; Chen, C. X.; Swager, T. M.; Hadjichristidis, N.; Xenidou, M.; Fetters, L. J.; Joannopoulos, J. D.; Fink, Y.; Thomas, E. L. *Adv. Mater.* **2001**, *13*, 421–425.

(15) Yoon, J.; Lee, W.; Thomas, E. L. *MRS Bulletin* **2005**, *30*, 721–726.

(16) Alfrey, T.; Gurnee, E. F.; Schrenk, W. J. *Polym. Eng. Sci.* **1969**, *9*, 400–404.

(17) Lin, T.-P.; Chang, A. B.; Luo, S.-X.; Chen, H.-Y.; Lee, B.; Grubbs, R. H. *ACS Nano* **2017**, *11*, 11632–11641.

(18) Jeong, S. H.; Kim, J. M.; Baig, C. *Macromolecules* **2017**, *50*, 4491–4500.

(19) Dalsin, S. J.; Hillmyer, M. A.; Bates, F. S. *ACS Macro Lett.* **2014**, *3*, 423–427.

(20) Lohse, D. J.; Milner, S. T.; Fetters, L. J.; Xenidou, M.; Hadjichristidis, N.; Mendelson, R. A.; García-Franco, C. A.; Lyon, M. K. *Macromolecules* **2002**, *35*, 3066–3075.

(21) Gu, W.; Huh, J.; Hong, S. W.; Sveinbjornsson, B. R.; Park, C.; Grubbs, R. H.; Russell, T. P. *ACS Nano* **2013**, *7*, 2551–2558.

(22) Song, D.-P.; Li, C.; Colella, N. S.; Xie, W.; Li, S.; Lu, X.; Gido, S.; Lee, J.-H.; Watkins, J. J. *J. Am. Chem. Soc.* **2015**, *137*, 12510–12513.

(23) Xia, Y.; Kornfield, J. A.; Grubbs, R. H. *Macromolecules* **2009**, *42*, 3761–3766.

(24) Xia, Y.; Olsen, B. D.; Kornfield, J. A.; Grubbs, R. H. *J. Am. Chem. Soc.* **2009**, *131*, 18525–18532.

(25) Miyake, G. M.; Weitekamp, R. A.; Piunova, V. A.; Grubbs, R. H. *J. Am. Chem. Soc.* **2012**, *134*, 14249–14254.

(26) Miyake, G. M.; Piunova, V. A.; Weitekamp, R. A.; Grubbs, R. H. *Angew. Chem., Int. Ed.* **2012**, *51*, 11246–11248.

(27) Rizwan, A. M.; Dennis, L. Y. C.; Liu, C. *J. Environ. Sci.* **2008**, *20*, 120–128.

(28) Li, G.; Wang, L.; Ni, H.; Pittman, C., Jr. *J. Inorg. Organomet. Polym.* **2001**, *11*, 123–154.

(29) Cordes, D. B.; Lickiss, P. D.; Rataboul, F. *Chem. Rev.* **2010**, *110*, 2081–2173.

(30) Chae, C.-G.; Yu, Y.-G.; Seo, H.-B.; Kim, M.-J.; Grubbs, R. H.; Lee, J.-S. *Macromolecules* **2018**, *ASAP*.

(31) Piunova, V. A.; Miyake, G. M.; Daeffler, C. S.; Weitekamp, R. A.; Grubbs, R. H. *J. Am. Chem. Soc.* **2013**, *135*, 15609–15616.

(32) Urbas, A.; Fink, Y.; Thomas, E. L. *Macromolecules* **1999**, *32*, 4748–4750.

(33) Urbas, A.; Sharp, R.; Fink, Y.; Thomas, E. L.; Xenidou, M.; Fetters, L. J. *Adv. Mater.* **2000**, *12*, 812–814.

(34) Tanaka, H.; Hasegawa, H.; Hashimoto, T. *Macromolecules* **1991**, *24*, 240–251.

(35) Hashimoto, T.; Tanaka, H.; Hasegawa, H. *Macromolecules* **1990**, *23*, 4378–4386.

(36) Winey, K. I.; Thomas, E. L.; Fetters, L. J. *Macromolecules* **1991**, *24*, 6182–6188.

(37) Matsen, M. W. *Macromolecules* **1995**, *28*, 5765–5773.

(38) Macfarlane, R. J.; Kim, B.; Lee, B.; Weitekamp, R. A.; Bates, C. M.; Lee, S. F.; Chang, A. B.; Delaney, K. T.; Fredrickson, G. H.; Atwater, H. A.; Grubbs, R. H. *J. Am. Chem. Soc.* **2014**, 17374–17377.

(39) Tarascon, J. M.; Armand, M. *Nature* **2001**, *414*, 359–367.

(40) Goodenough, J. B.; Kim, Y. *Chem. Mater.* **2010**, *22*, 587–603.

(41) Hallinan, D. T.; Balsara, N. P. *Annu. Rev. Mater. Res.* **2013**, *43*, 503–525.

(42) Schulze, M. W.; McIntosh, L. D.; Hillmyer, M. A.; Lodge, T. P. *Nano Lett.* **2013**, *14*, 122–126.

(43) Young, W.-S.; Kuan, W.-F.; Epps, T. H. *J. Polym. Sci., Part B: Polym. Phys.* **2014**, *52*, 1–16.

(44) Agrawal, R. C.; Pandey, G. P. *J. Phys. D: Appl. Phys.* **2008**, *41*, 223001.

(45) Singh, M.; Odusanya, O.; Wilmes, G. M.; Eitouni, H. B.; Gomez, E. D.; Patel, A. J.; Chen, V. L.; Park, M. J.; Fragouli, P.; Iatrou, H.; Hadjichristidis, N.; Cookson, D.; Balsara, N. P. *Macromolecules* **2007**, *40*, 4578–4585.

(46) Panday, A.; Mullin, S.; Gomez, E. D.; Wanakule, N.; Chen, V. L.; Hexemer, A.; Pople, J.; Balsara, N. P. *Macromolecules* **2009**, *42*, 4632–4637.

(47) Young, W.-S.; Albert, J. N. L.; Schantz, A. B.; Epps, T. H. *Macromolecules* **2011**, *44*, 8116–8123.

(48) Sun, J.; Stone, G. M.; Balsara, N. P.; Zuckermann, R. N. *Macromolecules* **2012**, *45*, 5151–5156.

(49) Cowie, J. M. G.; Sadaghianizadeh, K. *Solid State Ionics* **1990**, *42*, 243–249.

(50) Kuan, W.-F.; Remy, R.; Mackay, M. E.; Epps, T. H. *RSC Adv.* **2015**, *5*, 12597–12604.

(51) Zhang, Y.; Costantini, N.; Mierzwa, M.; Pakula, T.; Neugebauer, D.; Matyjaszewski, K. *Polymer* **2004**, *45*, 6333–6339.

(52) Lascaud, S.; Perrier, M.; Vallee, A.; Besner, S.; Prud'homme, J.; Armand, M. *Macromolecules* **1994**, *27*, 7469–7477.

(53) Zhao, C.; Wu, D.; Huang, N.; Zhao, H. *J. Polym. Sci., Part B: Polym. Phys.* **2008**, *46*, 589–598.
(54) Yuan, R.; Teran, A. A.; Gurevitch, I.; Mullin, S. A.; Wanakule, N. S.; Balsara, N. P. *Macromolecules* **2013**, *46*, 914–921.
(55) Teran, A. A.; Mullin, S. A.; Hallinan, D. T.; Balsara, N. P. *ACS Macro Lett.* **2012**, *1*, 305–309.
(56) Bouchet, R.; Phan, T. N. T.; Beaudoin, E.; Devaux, D.; Davidson, P.; Bertin, D.; Denoyel, R. *Macromolecules* **2014**, *47*, 2659–2665.
(57) Young, N. P.; Devaux, D.; Khurana, R.; Coates, G. W.; Balsara, N. P. *Solid State Ionics* **2014**, *263*, 87–94.
(58) Gomez, E. D.; Panday, A.; Feng, E. H.; Chen, V.; Stone, G. M.; Minor, A. M.; Kisielowski, C.; Downing, K. H.; Borodin, O.; Smith, G. D.; Balsara, N. P. *Nano Lett.* **2009**, *9*, 1212–1216.
(59) Ganesan, V.; Pyramitsyn, V.; Bertoni, C.; Shah, M. *ACS Macro Lett.* **2012**, *1*, 513–518.
(60) Hou, W.-H.; Chen, C.-Y.; Wang, C.-C.; Huang, Y.-H. *Electrochim. Acta* **2003**, *48*, 679–690.
(61) Chintapalli, M.; Chen, X. C.; Thelen, J. L.; Teran, A. A.; Wang, X.; Garetz, B. A.; Balsara, N. P. *Macromolecules* **2014**, *47*, 5424–5431.
(62) Pakula, T.; Zhang, Y.; Matyjaszewski, K.; Lee, H.-i.; Boerner, H.; Qin, S.; Berry, G. C. *Polymer* **2006**, *47*, 7198–7206.
(63) Quartarone, E.; Mustarelli, P. *Chem. Soc. Rev.* **2011**, *40*, 2525–2540.
(64) Armand, M.; Endres, F.; MacFarlane, D. R.; Ohno, H.; Scrosati, B. *Nat. Mater.* **2009**, *8*, 621–629.
(65) Ye, Y.-S.; Rick, J.; Hwang, B.-J. *J. Mater. Chem. A* **2013**, *1*, 2719–2743.
(66) Welton, T. *Chem. Rev.* **1999**, *99*, 2071–2084.
(67) Galiński, M.; Lewandowski, A.; Stępniak, I. *Electrochim. Acta* **2006**, *51*, 5567–5580.
(68) Lee, K. H.; Zhang, S.; Lodge, T. P.; Frisbie, C. D. *J. Phys. Chem. B* **2011**, *115*, 3315–3321.
(69) Fullerton-Shirey, S. K.; Maranas, J. K. *Macromolecules* **2009**, *42*, 2142–2156.
(70) He, Y.; Boswell, P. G.; Bühlmann, P.; Lodge, T. P. *J. Phys. Chem. B* **2007**, *111*, 4645–4652.
(71) Seitz, M. E.; Burghardt, W. R.; Faber, K. T.; Shull, K. R. *Macromolecules* **2007**, *40*, 1218–1226.
(72) Heimenz, P. C.; Lodge, T. P. *Polymer Chemistry*; 2nd ed.; CRC Press: Boca Raton, FL, 2007.
(73) Hu, M.; Xia, Y.; McKenna, G. B.; Kornfield, J. A.; Grubbs, R. H. *Macromolecules* **2011**, *44*, 6935–6943.
(74) Dalsin, S. J.; Hillmyer, M. A.; Bates, F. S. *Macromolecules* **2015**, *48*, 4680–4691.
(75) Zhang, S.; Lee, K. H.; Frisbie, C. D.; Lodge, T. P. *Macromolecules* **2011**, *44*, 940–949.
(76) Susan, M. A. B. H.; Kaneko, T.; Noda, A.; Watanabe, M. *J. Am. Chem. Soc.* **2005**, *127*, 4976–4983.
(77) Tang, B.; White, S. P.; Frisbie, C. D.; Lodge, T. P. *Macromolecules* **2015**, *48*, 4942–4950.

(78) McNicholas, B. J.; Blakemore, J. D.; Chang, A. B.; Bates, C. M.; Kramer, W. W.; Grubbs, R. H.; Gray, H. B. *J. Am. Chem. Soc.* **2016**, *138*, 11160–11163.
(79) Hawecker, J.; Lehn, J.-M.; Ziessel, R. *J. Chem. Soc., Chem. Commun.* **1983**, 536–538.
(80) Hawecker, J.; Lehn, J.-M.; Ziessel, R. *J. Chem. Soc., Chem. Commun.* **1984**, 328–330.
(81) Blakemore, J. D.; Gupta, A.; Warren, J. J.; Brunschwig, B. S.; Gray, H. B. *J. Am. Chem. Soc.* **2013**, *135*, 18288–18291.